Journal of Materials Chemistry A

ROYAL SOCIETY OF CHEMISTRY

PAPER

View Article Online
View Journal

Cite this: DOI: 10.1039/d0ta03080e

Inexpensive thermochemical energy storage utilising additive enhanced limestone†

Kasper T. Møller, * Ainee Ibrahim, Craig E. Buckley and Mark Paskevicius *

Energy storage is one of the key challenges in our society to enable a transition to renewable energy sources. The endothermic decomposition of limestone into lime and CO_2 is one of the most cost-effective energy storage systems but it significantly degrades on repeated energy cycling (to below 10% capacity). This study presents the first $CaCO_3$ system operating under physical conditions that mimic a real-life 'thermal battery' over an extended cycling life. These important results demonstrate that a thermal energy storage device based on $CaCO_3$ will be suitable for a range of applications, *e.g.* concentrated solar power plants, wind farms, photovoltaics, and excess grid energy. The operating temperature of 900 °C ensures a higher Carnot efficiency than state-of-the-art technologies at a fraction of the material cost. The capacity degradation of pure $CaCO_3$ as a function of calcination/carbonation cycling is overcome by the addition of either ZrO_2 (40 wt%) or Al_2O_3 (20 wt%), which results in 500 energy storage cycles at over 80% capacity. The additives result in the formation of ternary compounds, *e.g.* $CaZrO_3$ and $Ca_5Al_6O_{14}$, which restrict sintering and allow for the transmission of Ca^{2+} and O^{2-} ions to reaction sites.

Received 18th March 2020
Accepted 27th April 2020

DOI: 10.1039/d0ta03080e

rsc.li/materials-a

Introduction

The relatively low operating temperature and low energy density (<413 kJ kg^{-1}) of molten salt technology results in a high concentrated solar power (CSP) energy storage cost. Despite having energy storage costs lower than Li-ion batteries, improvements are required to enable higher operating temperature and efficiency at a lower cost.[1] Thermal batteries offer a direct alternative to electrochemical batteries for excess renewable energy storage and load levelling.

Various materials have been suggested as the successor to molten salt,[2] including gas–solid based thermochemical energy storage (TCES) materials such as metal carbonates, which have high energy densities (>1000 kJ kg^{-1}) making them attractive.[1,3,4] Utilisation of $CaCO_3$ as a TCES material was proposed in the 1970s.[5] However, the major technical issue that has not yet been adequately solved is the degradation of its CO_2 storage capacity over many cycles of gas release and absorption when used for heat storage. A previous study highlights how the CO_2 capacity in $CaCO_3$ drops to only ~8% of its initial capacity after 500 cycles, which is exacerbated by high calcination temperatures.[6] The cause of the capacity loss has been attributed to: a loss of porosity in formed CaO, sintering of $CaCO_3$, and limited CO_2 diffusion through $CaCO_3$, which has been shown to form a shell-like structure around unreacted CaO.[5,7,8] As such, research must be directed towards overcoming the technical challenges associated with using $CaCO_3$ as an energy storage material near 900 °C. The 1 bar CO_2 equilibrium pressure is at 890 °C for $CaCO_3$, dictated by the thermodynamics:[9]

$$CaCO_3 \leftrightarrow CaO + CO_2(g),\ \Delta H_{890\ ^\circ C} = 165.7\ kJ;\ \Delta S_{890\ ^\circ C} = 143.0\ J\ K^{-1};\ \Delta G_{890\ ^\circ C} \approx 0\ kJ \quad (1)$$

Predominantly, research has focused on using metal oxides and other minerals for carbon capture rather than thermal energy storage.[4,10] Most studies only investigate the reactions between CaO and carbon dioxide at low concentration and gas pressure (≤1 bar), usually at moderate temperatures (650–850 °C) for CO_2 sequestration purposes.[11] Hence, the conditions are not suitable for a thermal battery as described here, and the development of TCES systems based on these materials has been investigated to a lesser degree.[12] As such, it is critical to assess the $CaCO_3$ thermochemical system at operating temperatures above 890 °C and CO_2 pressures above 1 bar since the rate of CO_2 release (and energy release) is strongly dependent on gas pressure,[13] while temperature greatly influences the system's reversibility.[14] The key issue of CaO and/or $CaCO_3$ sintering at high temperatures could be minimised though the addition of additives to separate active components and minimise agglomeration, for instance through the addition of MgO.[15] Other additives are known to react with either $CaCO_3$ or CaO at high temperature to form ternary compounds, *e.g.* $CaSiO_3$ and $CaZrO_3$.[16,17] Cyclic stability has been achieved in the

Fuels and Energy Technology Institute, Curtin University, GPO Box U1987, Perth 6845, WA, Australia. E-mail: kasper.moller@curtin.edu.au; mark.paskevicius@gmail.com

† Electronic supplementary information (ESI) available. See DOI: 10.1039/d0ta03080e

$CaCO_3$ system for sequestration purposes after the addition of aluminium oxide, iron oxide, or zirconium oxide,[11,18,19] where binary compounds appear to act as active catalysts. However, the operating conditions often involve: (i) low-temperature carbonation (T < 750 °C) that would restrict agglomeration and thus do not present the same obstacles as faced in this study and (ii) few cycles (<20), which are not representative of a long-term energy storage solution.

Experimental

Sample preparation

$CaCO_3$ was mixed with additives in a 20 wt% ratio (4 g $CaCO_3$ and 1 g of additive), except $BaCO_3$, which was added in a 5 mol% ratio. 10 mL of ethanol (CH_3CH_2OH) was added and the mixtures were ball-milled in stainless steel vials for 2 hours (15 min milling × 1 min pause × 8 reps; 12 × 8 mm od. stainless steel balls). After ball-milling, the samples were dried in an oven at 105 °C for approximately 1 hour to obtain a dry powder. Note, that the above procedure was carried out in an argon-filled glovebox for the Ni sample, which was dried by applying dynamic vacuum. Additional ratios were produced for $CaCO_3$–ZrO_2 and $CaCO_3$–Al_2O_3, *i.e.* 10 and 40 wt%, hence 4.5 g $CaCO_3$ and 0.5 g additive, or 3 g $CaCO_3$ and 2 g additive, respectively, were ball-milled using the same procedure. Finally, a sample of $CaCO_3$–20 wt% ZrO_2 (~4 g and ~1 g, respectively) was ball-milled for a total of 10 hours (20 min milling × 2 min pause × 30 reps) in a ZrO_2 vial using 12 × 1 mm od. ZrO_2 balls, to obtain a small particle size sample. Various additives were chosen to isolate CaO particles and prevent sintering (Table S1†).

Thermogravimetric and differential scanning calorimetry

Thermogravimetric and simultaneous differential scanning calorimetry (TG-DSC) were performed on a Mettler Toledo DSC 1 instrument. The samples were heated from room temperature to 1000 °C ($\Delta T/\Delta t$ = 10 °C min^{-1}) under an argon flow (20 mL min^{-1}).

Sieverts' method gas studies

Samples were introduced into a SiC sample cell, which was attached *via* Swagelok parts to a Hy-Energy PCTpro E&E.[20] The sample was heated to ~900 °C ($\Delta T/\Delta t$ = 5 °C min^{-1}) at $p(CO_2) = 10^{-2}$ bar, hence decomposing the sample. Subsequently, cycling of the sample was initiated at isothermal conditions (~900 °C) with carbonation at $p_{ini}(CO_2) \sim 6$ bar for 30 minutes in a 46.3 cm^3 volume, followed by calcination at $p_{ini}(CO_2) \sim 10^{-2}$ bar for 20 minutes in a 206.7 cm^3 volume. A total of 50 cycles was collected for all samples. Finally, the samples were carbonated and cooled to room temperature under $p(CO_2) \sim 5$ bar. The data has been corrected to account for the 80 wt% $CaCO_3$ quantity, which is the active component, while the graphs and fractional capacity are based on 1 mol of CO_2 being released/absorbed according to reaction scheme (1).

Additional experiments were conducted for the additives ZrO_2 and Al_2O_3, including extended experiments for ≥100 cycles using the same conditions as above. However, the Al_2O_3 (20 wt%) was cycled for 500 cycles while varying the calcination/carbonation times between 20 minutes/30 minutes and up to 12 hours each. The carbonation time was further extended up to 96 hours to 'regenerate' the sample.

Finally, the data were treated manually and compressibility factors were extracted from REFPROP.[21]

Powder X-ray diffraction

X-ray diffraction (XRD) on powdered samples was performed on a Bruker D8 Advance diffractometer equipped with a CuK$\alpha_{1,2}$ source in flat-plate geometry mode. Data were collected using a Lynxeye PSD detector from 15–70° 2θ at 0.02° steps.

***In situ* synchrotron radiation powder X-ray diffraction.** *In situ* time-resolved Synchrotron Radiation X-ray Diffraction (SR-XRD) data was collected at the Powder Diffraction beamline at the Australian Synchrotron, Melbourne, Australia on a Mythen microstrip detector at λ = 0.82502 Å.[22,23] Powdered samples were loaded into quartz capillaries (i.d. = 0.5 mm, o.d. = 0.6 mm), which were attached to a gas system enabling control of CO_2 pressure. The samples were heated by a heat blower to 950 °C at $\Delta T/\Delta t$ = 6 °C min^{-1} while oscillating during data acquisition. Temperature calibrations were performed using the well-known thermal expansion of NaCl and Ag.[24,25]

Scanning electron microscopy

Scanning electron microscopy (SEM) and energy dispersive spectroscopy (EDS) were performed using a Tescan Mira3 FESEM with an Oxford Instruments X-Max SDD X-ray detector and AZtec software. The SEM images were collected using a backscattered electrons detector, an accelerating voltage of 15 kV, an aperture size of 30 μm, and a working distance of ~15 mm. SEM samples were prepared by embedding powdered samples in an epoxy resin, which was polished using colloidal silica. Eventually the polished samples were sputter-coated with a 10 nm thick carbon layer.

Small angle X-ray scattering

Small angle X-ray scattering data were collected on a Bruker Nanostar instrument equipped with an Excillium MetalJet source (GaK$_\alpha$, λ = 1.3402 Å). Sample powders were pressed between tape in transmission geometry and measured under vacuum. Data were background subtracted and put onto an absolute scale using a NIST SRM3600 glassy carbon standard.[26] Specific surface area (SSA) was calculated from the high-q Porod region (power law slope = 4) using the Unified model in the Irena software package for Igor Pro (WaveMetrics).[27,28] This is calculated through:

$$\mathrm{SSA} = \frac{B}{2\pi\delta\Delta\rho^2}$$

where B is Porod's constant refined in the unified fit, δ is the crystallographic density, and $\Delta\rho^2$ is the scattering contrast.

Results & discussion

Cyclic stability for different additives

Eleven different additive-enhanced $CaCO_3$ samples were prepared as given in Table S1.† The thermal properties and cyclic CO_2 capacity over 50 one-hour cycles are summarised in Table S2,† and Fig. 1a. Initial thermal analysis of the samples shows no thermodynamic destabilisation of $CaCO_3$, but some kinetic modifications to the first calcination, see Fig. S1 and S2.† A rapid capacity retention screening of the additive-enhanced $CaCO_3$ (1 hour calcination/carbonation at 900 °C) generally shows that the CO_2 capacity decreases dramatically within the first 10 cycles and eventually most of the samples retain a lower cyclic capacity than the pristine $CaCO_3$ sample due to side reactions. Pristine $CaCO_3$ reaches ~14% of the theoretical CO_2 capacity after 50 calcination/carbonation cycles, similar to previous studies.[29] A few of the additive-enhanced $CaCO_3$ systems show promise to improve the cyclic stability of the $CaCO_3$.

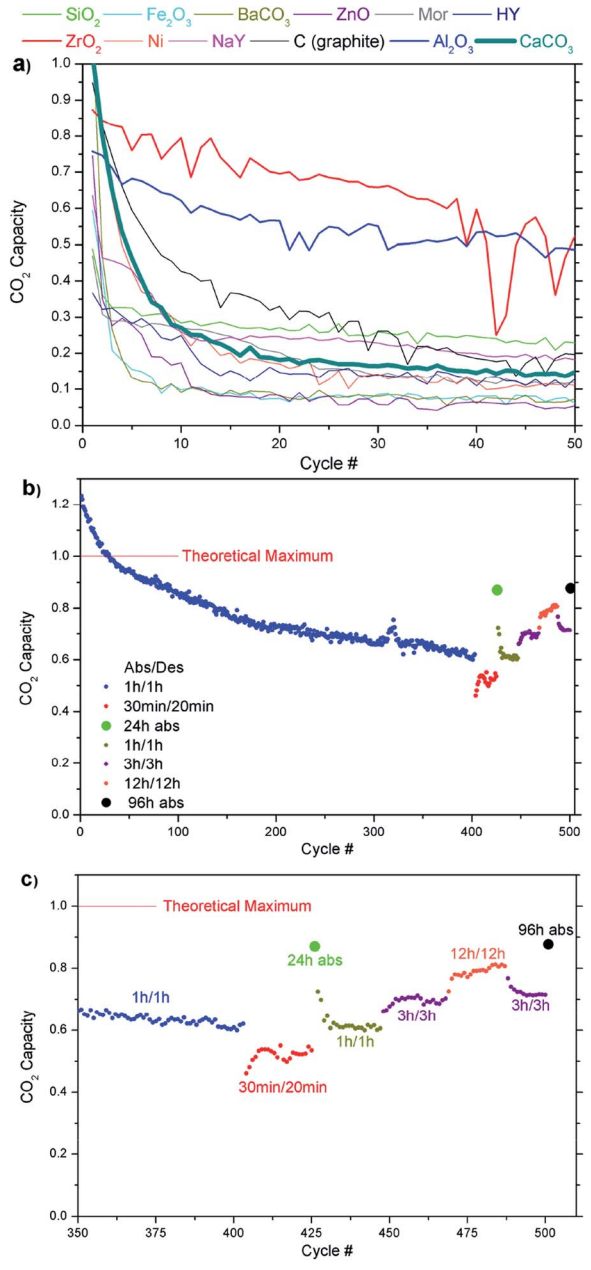

Fig. 1 (a) Carbonation data of additive-enhanced $CaCO_3$ systems over 50 calcination–carbonation cycles ($t_{abs/des}$ = 1 hour) at 900 °C, highlighting Al_2O_3 (20 wt%) and ZrO_2 (20 wt%) as the most promising additives. All additives are 20 wt% except $BaCO_3$, which was 5 mol% (see Table S1†). (b & c) Absorption data of $CaCO_3$–Al_2O_3 (20 wt% bulk) over 500 calcination–carbonation cycles with varying calcination/carbonation times. The theoretical maximum refers to the $CaCO_3$ remaining (59.1%) after assuming a full reaction with the 20 wt% Al_2O_3 additive into $Ca_5Al_6O_{14}$ (reaction scheme (3)).

The SiO_2 and NaY additives react with $CaCO_3$ to form spurrite ($Ca_5(SiO_4)_2CO_3$), and during cycling they both stabilise at ≈16–20% of the expected CO_2 capacity, which is slightly better than the pure $CaCO_3$ sample. Graphite addition aids in a slower CO_2 capacity loss, however, after 50 cycles the capacity is similar to SiO_2 and NaY at 20%. See ESI† for further information on these systems. Indeed, the most promising additives are Al_2O_3 and ZrO_2, and thus these will be the focus of this study. The addition of 20 wt% ZrO_2 retains a CO_2 capacity of ~80% within the first 10 cycles, but a steady degradation of the sample is observed and at the end of 50 one-hour cycles the CO_2 capacity is reduced to ~55%. Similarly, the addition of 20 wt% Al_2O_3 results in a steady capacity degradation, and after 50 CO_2 cycles, it reaches ~49% of the expected capacity. It should be emphasised that the cyclic capacity is heavily reliant on the kinetics of CO_2 release and absorption, and one-hour cycles do not always allow for complete reactions to occur.

Optimising the additives

To further improve the CO_2 (and energy) storage capacity, samples of varying weight ratios of ZrO_2 (20 & 40 wt%) and Al_2O_3 (10, 20 & 40 wt%) were investigated, see Table S1.† The addition of 40 wt% ZrO_2 provides superior CO_2 capacity compared to 20 wt% ZrO_2 (Fig. S3†), but at the detriment of the remaining quantity of active component ($CaCO_3$). Extended ball-milling (ten hours instead of two hours) of the 20 wt% ZrO_2 sample was undertaken to result in smaller particles and better mixing. However, the long ball-milling results in the same trend in CO_2 capacity loss as the two-hour ball-milled sample. Hence, an initially smaller particle size does not influence the overall CO_2 capacity after 50 cycles.

The optimum quantity of Al_2O_3 to add was found to be 20 wt% Al_2O_3 with a CO_2 capacity of ~49% after 50 one-hour cycles (Fig. S4†). Here, a 10 wt% Al_2O_3 loading is insufficient to retain CO_2 capacity and a 40 wt% loading causes CO_2 capacity to drop below 10% within the first 10 cycles. In a similar manner to ZrO_2, starting from either bulk or nanoparticle (13 nm) Al_2O_3 results in no measurable change in the CO_2 capacity loss during cycling. Hence, using low-cost bulk Al_2O_3 is preferable in the application.

Extended cycling and the influence of calcination/carbonation time

The optimised $CaCO_3$–Al_2O_3 (20 wt%) system was CO_2 cycled 500 times at 900 °C for varying calcination/carbonation times,

see Fig. 1b and c. The capacity retention after 500 cycles is ≥80% when carbonation times are extended to ≥12 hours. It is important to note that the theoretical maximum (1 mole of CO_2, 100%) is calculated based on the assumption that reaction 3 fully occurs. However, it is observed that this reaction is not completed until the 30th cycle. Hence, the CO_2 capacity exceeds the theoretical capacity within the first 30 cycles as more $CaO/CaCO_3$ is available for reaction during these cycles until $Ca_5Al_6O_{14}$ is completely formed. Additionally, the response time for gas absorption/desorption is shown by the high CO_2 capacity (~60%) even for one-hour cycles of calcination and carbonation. This is mirrored in the rapid 30 and 20 minute cycles that maintain a 50% CO_2 capacity, while longer cycling times result in capacities from 80–90%. Hence, the $CaCO_3$–Al_2O_3 (20 wt%) system shows remarkable energy storage properties: response time and capacity, which makes this system suitable for a thermal battery. Finally, the heat release/uptake should be mentioned. Temperature spikes are observed from a thermocouple in the sample reactor when absorption and desorption is initiated with $\Delta T \pm 1$ °C. Considering the sample mass (~250 mg), this temperature excursion suggests rapid heat (energy) release/uptake (see Fig. S5†), which is dissipated through the thermal conductivity of $CaO/CaCO_3$, which has recently been reported.[30] The temperature spikes are more distinct on carbonation, probably due to active counteraction from the furnace to maintain the temperature at 900 °C on calcination.

Reaction kinetics of $CaCO_3$–Al_2O_3 (20 wt%) calcination/carbonation

A comparison of the reaction kinetics at the initial, middle, and final stage of all samples during the 50 one-hour calcination/carbonation cycles is given in Fig. S6.† Two different reaction stages are observed during CO_2 absorption with the reaction kinetics being much faster in the first step compared to the second. This two-stage reaction limiting process has previously been assigned to the diffusion coefficients of CO_2 through the CaO layer (rapid) and the formed $CaCO_3$ layer (slow): $D_{CaO} = 0.3\ cm^2\ s^{-1}$ and $D_{CaCO_3} = 0.003\ cm^2\ s^{-1}$.[5] Hence, as $CaCO_3$ is formed on the surface of the CaO particles, reaction kinetics decrease due to the lower diffusion coefficient through $CaCO_3$. Thus, CO_2 absorption having to propagate from the outside to the inside of a particle through a $CaCO_3$ shell is prolonged, whereas CO_2 release can initiate from the outside shell of $CaCO_3$ and hence diffuse through CaO, not $CaCO_3$, which is fast. However, in this study the rate of calcination is much slower than for carbonation, which is not clearly described by only a $CaCO_3$ shell that inhibits CO_2 absorption. The gradual CO_2 desorption would not be affected by a $CaCO_3$ shell and is instead assigned to the low pressure differential between the equilibrium pressure (1.2 bar at 900 °C) and the operating pressure during CO_2 release (~0.7 bar). Faster reaction kinetics are observed during carbonation because it is performed at a significant overpressure (~5 bar) compared to the equilibrium pressure. Thus, reaction kinetics can be improved by increasing the differential pressure between the equilibrium pressure and operating pressure. Despite the kinetic complexity, it is clear that the calcination of bulk $CaCO_3$ is slower than for the additive enhanced samples, *i.e.* containing ZrO_2 and Al_2O_3, which may be related to the faster diffusion through the ternary compounds than through $CaCO_3$.

Active components and hypothesised reaction mechanism

A comparison of the crystalline compounds in the additive-enhanced $CaCO_3$ samples and the resulting carbonated samples after 50 calcination/carbonation cycles reveals that non-reversible side reactions occur between the additives and the $CaCO_3$ at high temperature, partly explaining the decreasing CO_2 capacity, see Fig. S7–S17.† Fig. S7† shows powder X-ray diffraction (XRD) data of the $CaCO_3$–ZrO_2 (20 wt%) and $CaCO_3$–Al_2O_3 (20 wt%) samples, which highlights that a non-reversible reaction between $CaCO_3/CaO$ and the additive has occurred, see reaction scheme (2) and (3):

$$CaO(s) + ZrO_2(s) \rightarrow CaZrO_3(s) \quad (2)$$

$$5CaO(s) + 3Al_2O_3(s) \rightarrow Ca_5Al_6O_{14}(s) \quad (3)$$

$$9CaO(s) + 3Al_2O_3(s) \rightarrow Ca_9Al_6O_{18}(s) \quad (4)$$

The ZrO_2 and Al_2O_3 enhanced $CaCO_3$ systems show cyclic capacities that are greatly enhanced compared to the other tested additives (Fig. 1). This makes it clear that a simple additive that only restricts $CaO/CaCO_3$ sintering is not the key to capacity retention. The important difference is, in fact, the properties of the as-formed ternary oxides, $CaZrO_3$ and $Ca_xAl_yO_z$. Parallel research studies into CO_2 sequestration and methane reforming have shown the benefits of certain additives including calcium zirconate and aluminate.[31–34] The feature that differentiates these ternary oxides from the other additives is their ability to conduct ions at high temperatures. Closely related $Ca_{12}Al_{14}O_{33}$ (Mayenite) is reported to be an oxide ion conductor,[35] and the layered structure of $Ca_5Al_6O_{14}$ is hypothesised to facilitate Ca^{2+} mobility.[36] O^{2-} and Ca^{2+} migration through the additive structure can thus improve reaction kinetics and be beneficial in retaining the CO_2 capacity.[17,37] The possibility of CaO migration is assigned to the low intrinsic defect formation energy of 1.61 eV to create a Ca-site Schottky-type disorder in $CaZrO_3$.[38]

Minor quantities of reaction side products, *i.e.* $CaAl_2O_4$ and $Ca_3Al_2O_6$ are observed after 50 CO_2 cycles, see Fig. S7.† Extending the study to 500 cycles reveals the conversion of side products into $Ca_5Al_6O_{14}$ and $Ca_9Al_6O_{18}$ (reaction scheme (4)) whilst a small fraction of Mayenite may also be present ($Ca_{12}Al_{14}O_{33}$, <3 wt% from Rietveld refinement, see Fig. S18†), see Fig. 2. Hence, the formation of $Ca_5Al_6O_{14}$ and $Ca_9Al_6O_{18}$ enables high stability in the cyclic capacity of the system compared to other investigated additives.[39] The crystal structure of $Ca_9Al_6O_{18}$ consists of Al_6O_{18} rings with a Ca^{2+} cation inside. However, only 72 of 80 available Ca^{2+} sites are occupied,[40] which is hypothesised to enable Ca^{2+} mobility through this crystal structure. The reaction mechanism is depicted in Fig. 3.

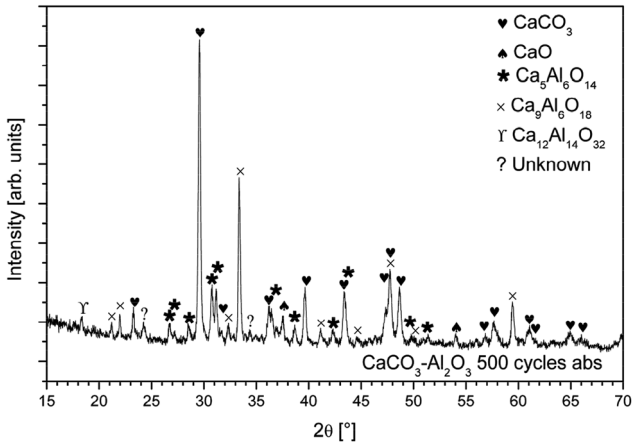

Fig. 2 XRD data ($\lambda = 1.54056$ Å) of $CaCO_3$–Al_2O_3 (20 wt%) absorbed after 500 calcination/carbonation cycles. The formation of the ternary compounds $Ca_5Al_6O_{14}$ and $Ca_9Al_6O_{18}$ is evident.

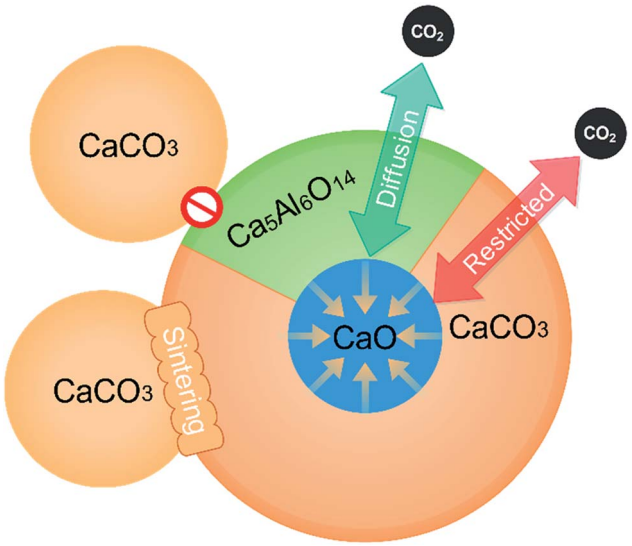

Fig. 3 Depiction of the reaction mechanism where Ca^{2+} and/or O^{2-} are able to migrate through the ternary compound and react at the surface with CO_2 to form $CaCO_3$ and generate thermal energy. The ternary compound also prevents sintering by acting as a barrier between regions of $CaCO_3$ and CaO.

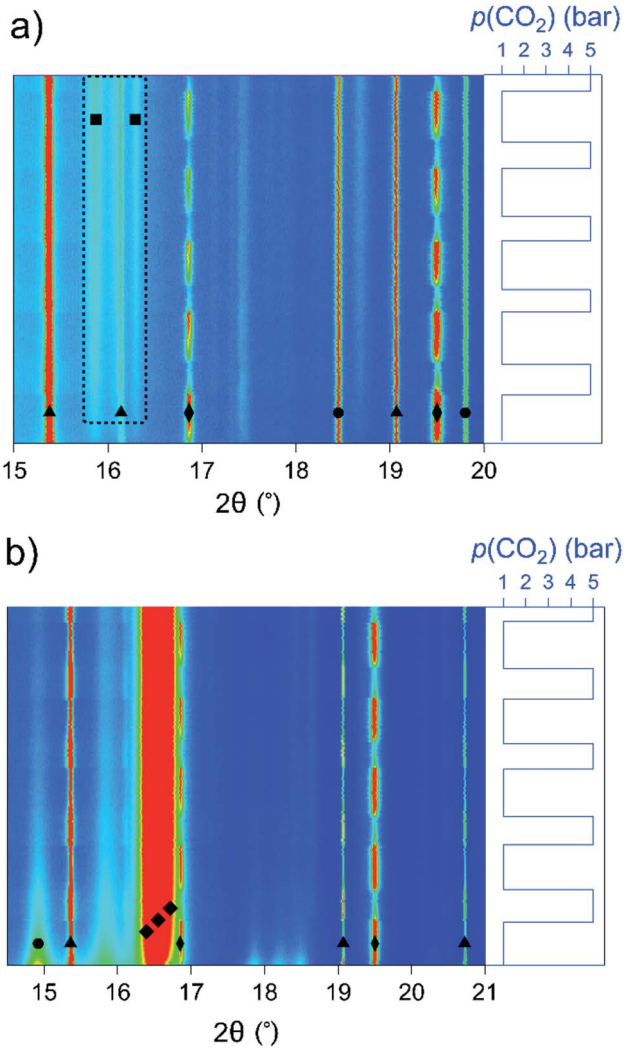

Fig. 4 (a) *In situ* SR-XRD data ($\lambda = 0.82502$ Å) of $CaCO_3$–Al_2O_3 (20 wt%, bulk) at 917 °C. Markers: triangle ($CaCO_3$); diamond (CaO); circle (Al_2O_3); square (Ca–Al–O compounds). The formation of Ca–Al–O compounds is highlighted by the dotted box. (b) *In situ* SR-XRD data of $CaCO_3$–ZrO_2 (40 wt%, bulk) at 917 °C. Markers: triangle ($CaCO_3$); diamond (CaO); circle (ZrO_2); squares ($CaZrO_3$). The pressure profile is indicated to the right of the respective figure. Carbonation was performed for ~20 min and calcination for ~30 min in a total of 5 cycles. Intensity is indicated as blue: low and red: high.

In situ phase analysis during CO_2 cycling

In situ synchrotron radiation X-ray diffraction (SR-XRD) data of $CaCO_3$–Al_2O_3 (20 wt%) was collected at 917 °C during CO_2 absorption (5 bar) and desorption (1 bar) cycling. The initial decomposition of $CaCO_3$ is evident by the formation of Bragg reflections from CaO, see Fig. 4a. Conversely, when CO_2 gas is applied to the system the CaO Bragg reflections decrease rapidly in intensity due to the reformation of $CaCO_3$. Throughout the 5 desorption/absorption cycles, Bragg reflections from Ca–Al–O containing compounds continue to increase in intensity, but do not completely react in the 5 cycles applied here. The prolonged formation of Ca–Al–O compounds agrees with the observations made in the gas sorption measurements, where it takes ~20 cycles before the consumption of Al_2O_3 is complete.

Fig. 4b shows the *in situ* SR-XRD cycling data of $CaCO_3$–ZrO_2 (40 wt%) at 917 °C. The immediate formation of $CaZrO_3$ and rapid depletion of ZrO_2 (within ~1 hour/1 cycle) is evident, and the amount of $CaZrO_3$ quickly reaches ~65 wt% of the sample (based on Rietveld refinement; theoretically 67.1 wt% at full reaction). Furthermore, the crystallite size of $CaCO_3$ and CaO doubles (to >200 and >125 nm, respectively, based on Rietveld refinement, see also Fig. S19 and S20†), over the 5 cycles applied here, which eventually may result in a capacity decrease due to large crystallites, see Table S3.† Despite the crystallite growth, the clear formation and consumption of CaO during CO_2 cycling shows the rapid response of the system to calcinate/carbonate.

Morphology

Scanning electron microscopy (SEM) was utilised to analyse the particle morphology of as-milled and CO_2 cycled samples, see Fig. 5. As-milled $CaCO_3$ consists of finely divided particles in the size range ~2 to 8 μm. The morphology significantly changes into a worm-like, porous structure after CO_2 cycling at 900 °C, with small crystalline particles on the surface of the 'worms', see Fig. S21.† The porosity should enable easy CO_2 access to the CaO particles; however, the worm-like morphology may retard carbonation through $CaCO_3$/CaO core–shell structure formation. The as-milled $CaCO_3$–Al_2O_3 sample consists of small particles (≤100 nm), which is assigned to the hardness of Al_2O_3 that may assist in creating smaller particles of $CaCO_3$ during milling. After cycling, the Al_2O_3 sample has turned into a rock-like morphology, with a degree of porosity, which allows CO_2 migration through the macro-structure. Furthermore, the as-milled $CaCO_3$–Al_2O_3 has specific regions that are aluminium (Al_2O_3) rich whereas the cycled sample shows that aluminium is well distributed after thermal treatment. Here, the aluminium is now combined with calcium in $Ca_5Al_6O_{14}$, which separates regions of CaO/$CaCO_3$ and is thus ascribed to prevent sintering. In the $CaCO_3$–ZrO_2 sample, the particle sizes range from small $CaCO_3$ particles (~1 to 5 μm) to larger ZrO_2 particles (~5 to 10 μm). From EDS mapping, the Zr seems reasonably well distributed in both the as-milled sample and after cycling, which is attributed to the fact that zirconium is present in each sample either as ZrO_2 or $CaZrO_3$. The extensive sintering observed may explain why the initial smaller particle size, *i.e.* extended ball-milling, does not influence the CO_2 cyclic capacity or reaction kinetics significantly. Small-angle X-ray scattering (SAXS) was utilised to determine the specific surface area of the ball-milled and cycled samples, see Fig. S22 and S23 and Table S4.† Generally, the samples show a low specific surface area between 1 and 5 $m^2\ g^{-1}$, which indicates a low degree of micro- or meso-porosity and thus supports the proposed mechanism of O^{2-} and Ca^{2+} migration through the solid material rather than CO_2 diffusion through porous channels. Only the as-milled samples containing nanoparticles of Al_2O_3 and ZrO_2 have larger specific surface areas of 29(3) and 52(5) $m^2\ g^{-1}$, respectively. In these cases, the specific surface area significantly decreases during cycling when particle size increases.

Perspectives and the promise of a thermal battery

A cost comparison of the proposed TCES materials, based on $CaCO_3$, and the state-of-the-art molten salt technology is provided in Table 1. A steep $3000 per tonne price for ZrO_2 makes the price per terajoule electrical energy in the $CaCO_3$–ZrO_2 (40 wt%) system expensive, and similar to the state-of-the-art molten salts. However, Al_2O_3 is more abundant and far more economical, *i.e.* $324 per tonne.[41] Hence, the materials cost can be reduced by ~95% per terajoule electrical energy produced if the molten salt is replaced with $CaCO_3$–Al_2O_3 (20 wt%). The operating pressure of <6 bar CO_2 reduces the engineering challenges and costs, whilst the CO_2 may be stored in a zeolite or activated carbon by physisorption, which avoids the energy penalty of CO_2 compression during storage.[42] Supercritical CO_2 may also be utilised as the heat transfer fluid at 900 °C,[43] which makes it compatible with the

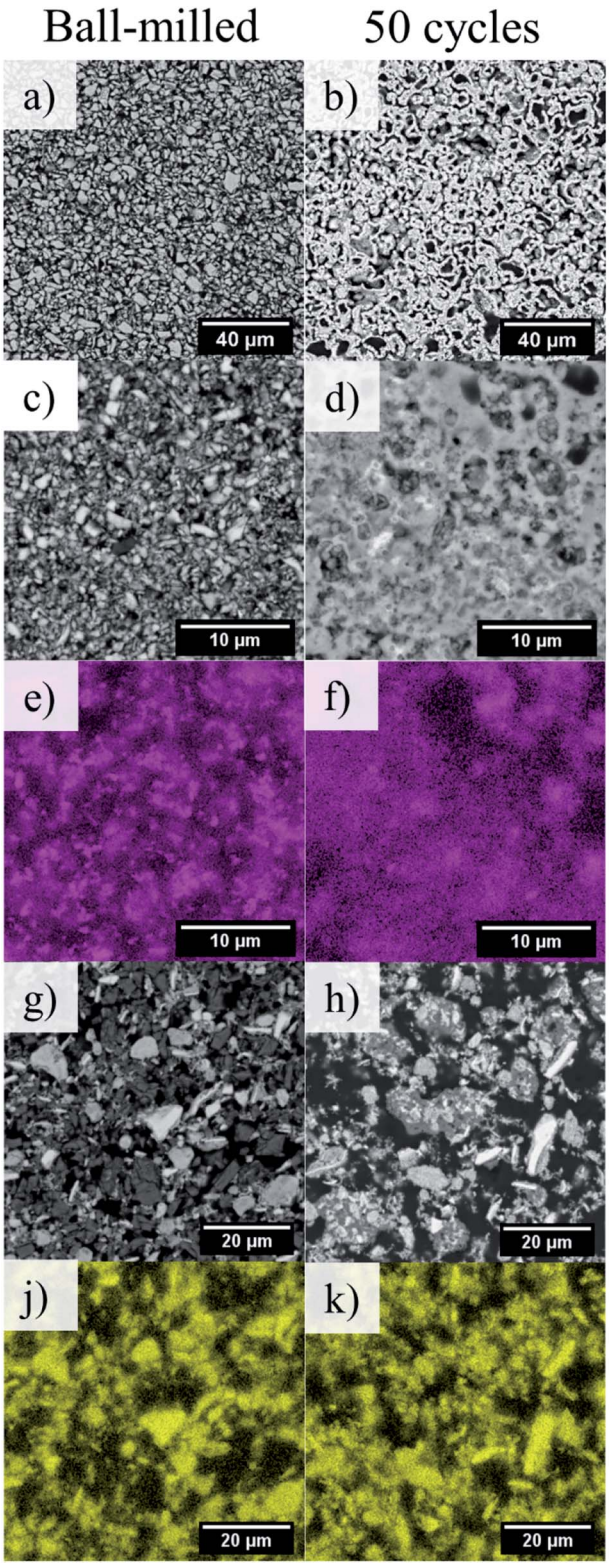

Fig. 5 Scanning electron microscopy data comparing the morphology of the as-milled samples (left column), the samples absorbed after 50 CO_2 cycles at 900 °C (right column), and energy dispersive spectroscopy showing the elemental distribution of aluminium and zirconium in the respective samples (Al: purple; Zr: yellow). a and b: $CaCO_3$; c–f: $CaCO_3$–Al_2O_3 (20 wt%); g–k: $CaCO_3$–ZrO_2 (40 wt%). The samples are embedded in epoxy resin and polished.

Table 1 Cost comparison of high-temperature thermal energy storage materials to store enough thermal energy to provide 1 TJ of electrical energy

	Molten salt ($40\ NaNO_3 : 60\ KNO_3$)	$CaMg(CO_3)_2 \rightleftarrows MgO + CaCO_3 + CO_2$	$CaCO_3 \rightleftarrows CaO + CO_2$	$CaCO_3 \rightleftarrows CaO + CO_2$ (40 wt% ZrO_2)	$CaCO_3 \rightleftarrows CaO + CO_2$ (20 wt% Al_2O_3)
Enthalpy ΔH (kJ mol^{-1})	39.0	125.8[a]	165.5[a]	165.5[a]	165.5[a]
Molar mass (g mol^{-1})	94.60	184.40	100.09	108.2	100.5
Density (g cm^{-3})[b]	2.17	2.85	2.71	3.43	2.89
Capacity (wt% CO_2)	—	23.9	44.0	26.4	35.2
Gravimetric energy density (kJ kg^{-1})	413	682	1657	455	782
Volumetric energy density (MJ m^{-3})[b]	895	1944	4489	1559	2257
Operating temperature range (°C)	290–565	~590	900	900	900
Carnot efficiency (%)[c]	46	65	74	74	74
Estimated practical efficiency (%)	27	41	49	49	49
Mass required (tonnes)[d]	9100	3598	1228	4470	2601
Volume required (m^3)[d]	4194	1262	453	1305	900
Materials cost ($ per tonne)[41,48,49]	630	50	10	1206	72.80
Total materials cost required (USD $)[d]	5 733 289	179 887	12 298	5 391 211	189 358
Assessment	− High cost	− Low efficiency	− Poor cycling capacity	− High cost	+ Low cost
	− Low efficiency	− High pressure	+ Low cost	+ Good kinetics	+ Good kinetics
	+ Established	− Poor kinetics	+ Low pressure	+ Low pressure	+ Low pressure
	+ No gas storage	+ Low cost			

[a] Per mol CO_2. [b] Based on crystalline data. [c] Lower temperature. [d] To generate 1 TJ of electrical energy.

Rankine–Brayton combined cycle or the Stirling engine for thermal to electrical energy conversion.[44] The latter is highly efficient at 900 °C (practically $\eta \sim 49\%$) and will work well on the kW scale.[45] Overall, the high energy density for $CaCO_3$–Al_2O_3 and its small footprint enables its utilisation in Stirling dishes, which are dispatchable concentrating solar thermal power systems that are ideal for remote areas, *e.g.* mine sites. Furthermore, a thermal battery enables seasonal or load-levelling storage of a variety of renewable energy from, *e.g.* wind farms, photovoltaics, and fossil fuel-based plants. A thermal battery based on $CaCO_3$–Al_2O_3, maintains an 80–90% capacity up to 500 cycles, with expectations for a 30-year lifetime. This is comparable to Li-ion batteries, which typically reaches a capacity of 80%, defined as the batteries cycle life, after 1000 to 4500 cycles, corresponding to a lifespan between 7 and 20 years.[3,46,47] Finally, a thermal battery based on $CaCO_3$ holds important intrinsic safety features: (i) the chemical reactions are limited by equilibrium pressure, which prevents the reactions from exceeding design conditions (ii) hot, corrosive fluids, *e.g.* molten salt, is not present (iii) the compounds are not flammable.

Conclusions

The $CaCO_3$–Al_2O_3 system presented here shows incomparable cyclic stability for CO_2 release and uptake over 500 cycles (>80%) at realistic operating conditions for utilisation in applications. The enhanced cyclability is assigned to the formation of ion-conducting Ca–Al–O compounds, *e.g.* $Ca_5Al_6O_{14}$ and $Ca_9Al_6O_{18}$. Due to a high enthalpy of formation for $CaCO_3$, this system is ideal for thermochemical energy storage. Both $CaCO_3$ and Al_2O_3 are cheap and abundant materials worldwide, resulting in an overall materials cost at only a fraction of state-of-the-art molten salt technologies (<4%). Furthermore, the system has a rapid response time with 60% of the full energy capacity stored or released within 1 hour, while the operating temperature of 900 °C ensures a high Carnot efficiency when converting the heat into electricity. The findings described here, enables $CaCO_3$ to be used as a thermal energy storage material in large-scale applications at realistic operating conditions. It is envisaged that thermal batteries could cover the requirements for bulk storage of renewable energy to cover the intermittent nature of the renewable energy sources and peak hour demand, or even enable energy production in remote areas outside the electricity grid.

Conflicts of interest

The contents of this disclosure is subject to patent protection as Australian Provisional Patent Application No. 2019904801.

Acknowledgements

KTM thanks The Independent Research Fund Denmark for International Postdoctoral Grant 8028-00009B. MP thanks the Australian Research Council for ARC Future Fellowship FT160100303. CEB, MP, and KTM acknowledge the Global Innovation Linkage project for grant GIL73589. CEB also acknowledges funding from ARC Linkage grant LP150100730. Nigel Chen-Tan is acknowledged for help in the laboratory. The

Powder Diffraction beamline at the Australian Synchrotron, Melbourne, Australia is acknowledged for the allocation of beamtime. Finally, SEM, PXD, and SAXS research was undertaken using the Tescan Mira3 EM (ARC LE130100053), the Bruker D8 Advance XRD instrumentation (ARC LE0775551), and the Bruker NanoStar SAXS instrument (ARC LE140100075) at the John de Laeter Centre, Curtin University. Dr Matthew Rowles is acknowledged for support with SAXS data collection.

References

1 T. D. Humphries, K. T. Møller, W. D. A. Rickard, M. V. Sofianos, S. Liu, C. E. Buckley and M. Paskevicius, *J. Mater. Chem. A*, 2019, **7**, 1206–1215.
2 M. Liu, N. H. Steven Tay, S. Bell, M. Belusko, R. Jacob, G. Will, W. Saman and F. Bruno, *Renewable Sustainable Energy Rev.*, 2016, **53**, 1411–1432.
3 K. T. Møller, D. Sheppard, D. B. Ravnsbæk, C. E. Buckley, E. Akiba, H.-W. Li and T. R. Jensen, *Energies*, 2017, **10**, 1645.
4 S. Kumar and S. K. Saxena, *Mater. Renewable Sustainable Energy*, 2014, **3**, 30.
5 R. Barker, *J. Appl. Chem. Biotechnol.*, 1973, **23**, 733–742.
6 G. S. Grasa and J. C. Abanades, *Ind. Eng. Chem. Res.*, 2006, **45**, 8846–8851.
7 V. Manovic and E. J. Anthony, *Energy Fuels*, 2010, **24**, 5790–5796.
8 J. C. Abanades and D. Alvarez, *Energy Fuels*, 2003, **17**, 308–315.
9 Outukumpu, *HSC Chemistry*, Houston, 1 edn, 2006, vol. 6.
10 A. A. Olajire, *J. Pet. Sci. Eng.*, 2013, **109**, 364–392.
11 A. M. Kierzkowska, R. Pacciani and C. R. Müller, *ChemSusChem*, 2013, **6**, 1130–1148.
12 A. J. Carrillo, J. González-Aguilar, M. Romero and J. M. Coronado, *Chem. Rev.*, 2019, **119**, 4777–4816.
13 E. P. Hyatt, I. B. Cutler and M. E. Wadsworth, *J. Am. Ceram. Soc.*, 1958, **41**, 70–74.
14 M. Zhao, Y. Song, G. Ji and X. Zhao, *Energy Fuels*, 2018, **32**, 5443–5452.
15 Q. Zhu, S. Zeng and Y. Yu, *Environ. Sci. Technol.*, 2017, **51**, 552–559.
16 M. Wang and C.-G. Lee, *Energy Convers. Manage.*, 2009, **50**, 636–638.
17 R. Angers, R. Tremblay and A. C. D. Chaklader, *J. Am. Ceram. Soc.*, 1972, **55**, 425.
18 C.-T. Yu and W.-C. Chen, *Fuel*, 2014, **122**, 179–185.
19 C.-T. Yu, S.-Y. Chen, W.-C. Chen and P.-H. Chang, *US Pat.* US20150093317A1, 2015.
20 D. A. Sheppard, M. Paskevicius, P. Javadian, I. J. Davies and C. E. Buckley, *J. Alloys Compd.*, 2019, **787**, 1225–1237.
21 E. W. Lemmon, *NIST Standard Reference Database 23: Reference Fluid Thermodynamic and Transport Properties—REFPROP*, 2013.
22 K. S. Wallwork, B. J. Kennedy and D. Wang, *AIP Conf. Proc.*, 2007, **879**, 879–882.
23 B. Schmitt, C. Brönnimann, E. F. Eikenberry, F. Gozzo, C. Hörmann, R. Horisberger and B. Patterson, *Nucl. Instrum. Methods Phys. Res., Sect. A*, 2003, **501**, 267–272.
24 B. R. S. Hansen, K. T. Møller, M. Paskevicius, A.-C. Dippel, P. Walter, C. J. Webb, C. Pistidda, N. Bergemann, M. Dornheim, T. Klassen, J.-E. Jørgensen and T. R. Jensen, *J. Appl. Crystallogr.*, 2015, **48**, 1234–1241.
25 J. Hu, W. Cai, C. Li, Y. Gan and L. Chen, *Appl. Phys. Lett.*, 2005, **86**, 151915.
26 O. Spalla, S. Lyonnard and F. Testard, *J. Appl. Crystallogr.*, 2003, **36**, 338–347.
27 G. Beaucage, *J. Appl. Crystallogr.*, 1995, **28**, 717–728.
28 J. Ilavsky and P. R. Jemian, *J. Appl. Crystallogr.*, 2009, **42**, 347–353.
29 P. E. Sánchez Jiménez, A. Perejón, M. Benítez Guerrero, J. M. Valverde, C. Ortiz and L. A. Pérez Maqueda, *Appl. Energy*, 2019, **235**, 543–552.
30 J. E. Bird, T. D. Humphries, M. Paskevicius, L. Poupin and C. E. Buckley, *Phys. Chem. Chem. Phys.*, 2020, **22**, 4617–4625.
31 C. Zhao, Z. Zhou, Z. Cheng and X. Fang, *Appl. Catal., B*, 2016, **196**, 16–26.
32 K. S. Sultana, D. T. Tran, J. C. Walmsley, M. Rønning and D. Chen, *Ind. Eng. Chem. Res.*, 2015, **54**, 8929–8939.
33 R. Koirala, K. R. Gunugunuri, S. E. Pratsinis and P. G. Smirniotis, *J. Phys. Chem. C*, 2011, **115**, 24804–24812.
34 P. Xu, Z. Zhou, C. Zhao and Z. Cheng, *Catal. Today*, 2016, **259**, 347–353.
35 M. Lacerda, J. T. S. Irvine, F. P. Glasser and A. R. West, *Nature*, 1988, **332**, 525–526.
36 M. Ruszak, S. Witkowski, P. Pietrzyk, A. Kotarba and Z. Sojka, *Funct. Mater. Lett.*, 2011, **04**, 183–186.
37 S. C. Hwang and G. M. Choi, *Solid State Ionics*, 2008, **179**, 1042–1045.
38 R. A. Davies, M. S. Islam and J. D. Gale, *Solid State Ionics*, 1999, **126**, 323–335.
39 Y. Hu, W. Liu, H. Chen, Z. Zhou, W. Wang, J. Sun, X. Yang, X. Li and M. Xu, *Fuel*, 2016, **181**, 199–206.
40 P. Mondal and J. W. Jeffery, *Acta Crystallogr., Sect. B: Struct. Crystallogr. Cryst. Chem.*, 1975, **31**, 689–697.
41 Alcoa, *Quarterly earnings Q3*, 2019, available at:https://investors.alcoa.com/financial-reports/quarterly-earnings/2019, accessed 11-02-2020.
42 L. Hauchhum and P. Mahanta, *Int. J. Energy Environ. Eng.*, 2014, **5**, 349–356.
43 Y. Ahn, S. J. Bae, M. Kim, S. K. Cho, S. Baik, J. I. Lee and J. E. Cha, *Nucl. Eng. Technol.*, 2015, **47**, 647–661.
44 V. Zare and M. Hasanzadeh, *Energy Convers. Manage.*, 2016, **128**, 227–237.
45 A. Bayon, R. Bader, M. Jafarian, L. Fedunik-Hofman, Y. Sun, J. Hinkley, S. Miller and W. Lipiński, *Energy*, 2018, **149**, 473–484.
46 J. B. Goodenough and K.-S. Park, *J. Am. Chem. Soc.*, 2013, **135**, 1167–1176.
47 G. L. Soloveichik, *Annu. Rev. Chem. Biomol. Eng.*, 2011, **2**, 503–527.
48 C. Y. Zhao, Y. Ji and Z. Xu, *Sol. Energy Mater. Sol. Cells*, 2015, **140**, 281–288.
49 U.S. Geological Survey, *Mineral Yearbook*, 2015, available at: https://s3-us-west-2.amazonaws.com/prd-wret/assets/palladium/production/mineral-pubs/stone-dimension/myb1-2015-stond.pdf, accessed 11-02-2020.

